Suporting Information
Simultaneous Enhancement of Charge Separation and Hole Transportation in a W:α-Fe_2O_3/MoS_2 Photoanode: The Collaborative Approach of MoS_2 as a Heterojunction and W as Metal Doping

Zohreh Masoumi[1], Meysam Tayebi[1], Morteza Kolaei[1], Ahmad Tayyebi[2], Hongsun Ryu[3] and Joon I. Jang[3]

Byeong-Kyu Lee[1,*]

[1]Department of Civil and Environment Engineering, University of Ulsan, Daehakro 93, Namgu, Ulsan 44610, Republic of Korea

[2]Department of Energy Engineering, School of Energy and Chemical Engineering, Ulsan National Institute of Science and Technology (UNIST), 50 UNIST-gil, Ulsan, 44919, Republic of Korea

[3]Department of Physics, Sogang University, 35 Baekbeom-ro, Mapo-gu, Seoul, 04107 South Korea
*Corresponding author: (bklee@ulsan.ac.kr)

Contents of Supplementary

1. Characterization Equipment

The morphologies and structures of the samples were characterized by using scanning electron microscopy (SEM, Model Quanta 250 FEG) and transmission electron microscopy (TEM, JEOL, JEM-2100F). The structures and crystallinities of the different catalytic films were characterized by X-ray diffraction (XRD). The X-ray source was Bruker D8Advance with monochromatic Cu Kα radiation (λ=1.5406 Å) in the 2θ range of 10–55°. A Raman spectrum was used with the laser line at 785 nm as the excitation source at room temperature (Bruker, model: Senteraa 2009, Germany). The chemical states of the component elements in the film samples were investigated using Thermo Scientific Sigma Probe spectrometer with a monochromatic AlKα source (photon energy 1486.6 eV), spot size of 400 μm, energy step size of 1.0 eV and pass energy of 200 eV. The optical properties of the photoanodes were measured by Perkin Elmer UV-Vis-NIR model Lambda 950. Finally, photoluminescence (PL) spectra were detected at room temperature using an Edinburgh F-4600 NF900 (FLS920) fluorescence spectrophotometer at an excitation of 400 nm. Electron paramagnetic resonance (EPR) measurements in the X-band (9.64 GHz) were performed using a CW/Pulse EPR System(QM09). The power 1 mW absorbed by the samples was recorded at room temperature. To measure the time-resolved photoluminescence (TRPL), we used the second harmonic generated beam of a Ti:sapphire laser (800 nm wavelength, 100 fs pulse-width, and 82 MHz repetition rate). The collected luminescence signal was dispersed by a monochromator (MS3504i, SOLAR TII) then detected by a photomultiplier tube (PMT-100, Becker & Hickl). The luminescence signal from the photomultiplier tube was processed by time-correlated single-photon counting (TCSPC) system (SPC-730, Becker & Hickl) to yield the temporal behavior of FTOs and hematite-based samples. The monitoring window for the TRPL measurements was 590 nm and 469 nm for FTOs and α-Fe_2O_3 s, respectively and the excitation intensity was about 4.7 MW/cm^2.

2. Calculation of parameters for MoS_2 nanosheets

The concentration (C_M), length (L), and thickness (N) of the exfoliated MoS_2 nanosheets was estimated by eq. S1, S2, and S3.

$$L(nm) = \frac{(3500 \times \frac{EXT_B}{EXT_{345}} - 140)}{(11.5 - \frac{EXT_B}{EXT_{345}})} \quad \text{(S1)}$$

$$C\ (mg.\ mL^{-1}) = EXT_{345}/(\alpha \times l) \quad \text{(S2)}$$

$$\text{Thickness (N (nm))} = 2.3 \times 10^{36} \times exp\left(-{}^{54888}/_{\lambda_A}\right) \quad \text{(S3)}$$

In equation S1, L is average size of nanosheets were estimated by EXT_B and EXT_{345} values in UV-vis data.

Concentration of the nanosheets in equation S2, depends on EXT_{345} value, the absorption coefficient (α), and the path length (l).

The equation S3 includes the wavelength of the absorbance light at A point (λ_A) which can be found in the UV-vis data (Fig.1a).

3. SEM and EDX of W doped samples

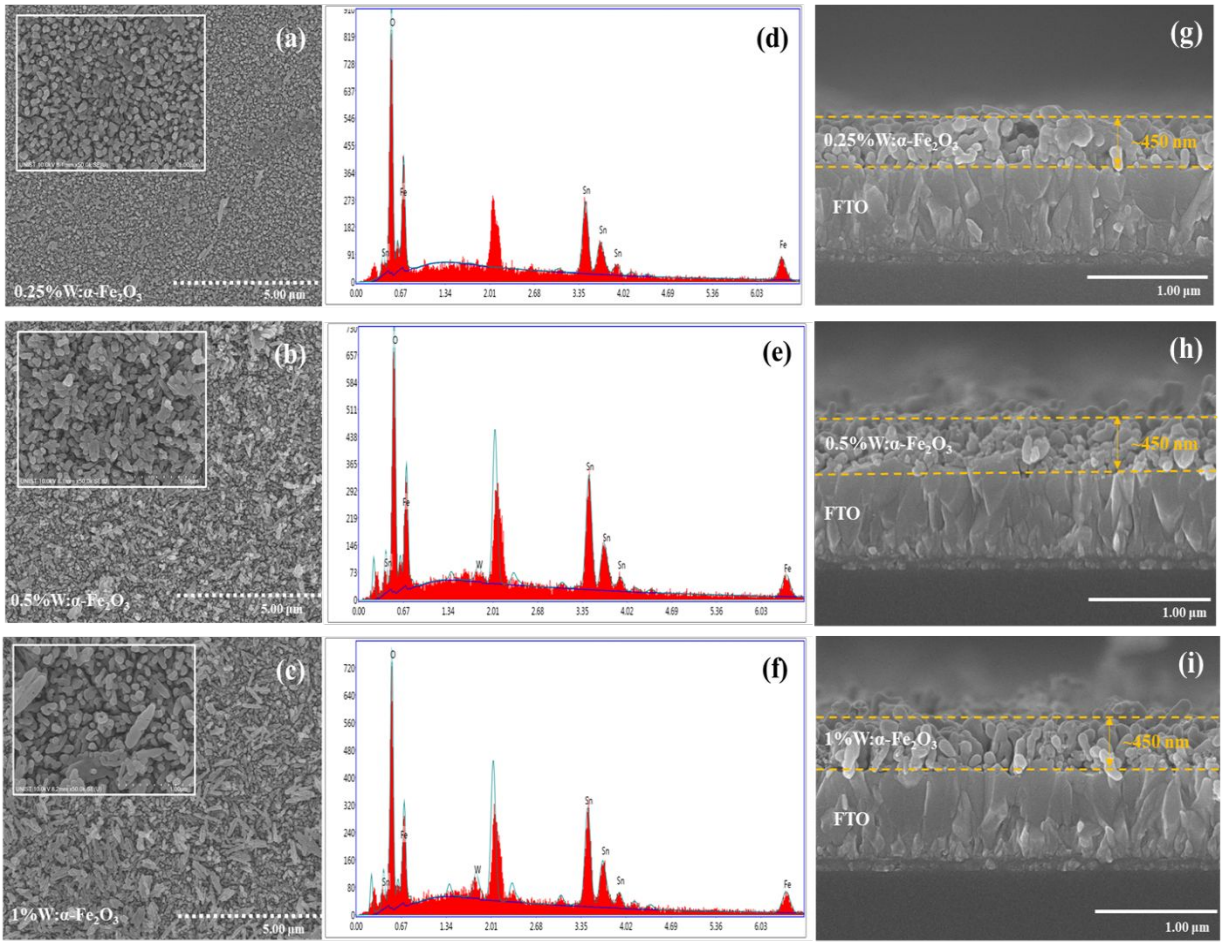

Fig. S1. (a-c) Top-view, (d-f) EDX, and (g-i) cross section of 0.25W:α-Fe_2O_3, 0.5W:α-Fe_2O_3, and 1W:α-Fe_2O_3 electrodes.

4. HRTEM and FFT for crystal structure

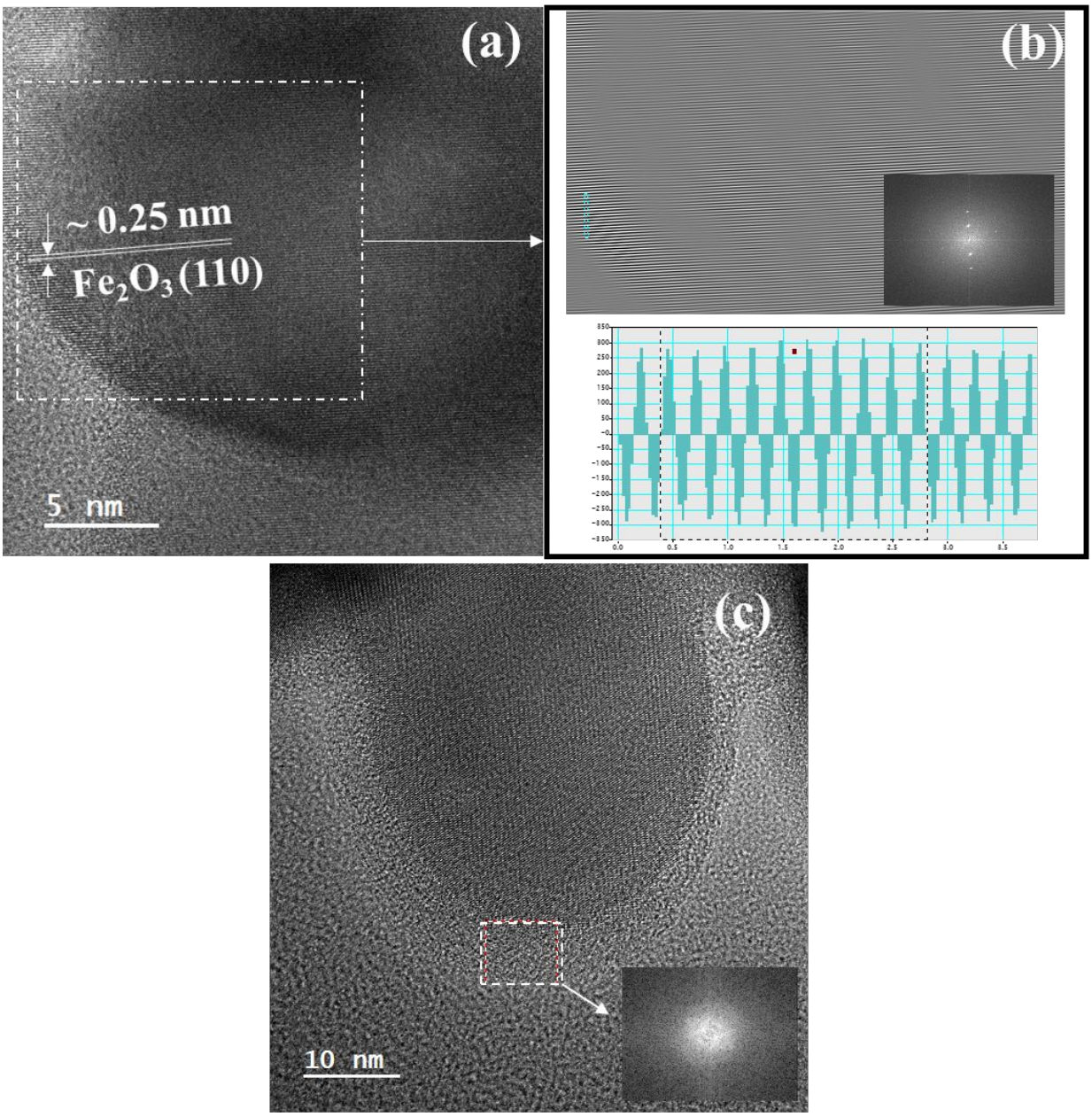

Fig. S2. (a) HRTEM image of 0.5W:α-Fe_2O_3, (b) FFT, inverse FFT, and profile of inverse FFT images of 0.5W:α-Fe_2O_3 , and (c) HRTEM image of 0.5W:α-Fe_2O_3/MoS_2 with FFT of MoS_2 layer.

5. XPS survey spectra for α-Fe_2O_3, 0.5W:α-Fe_2O_3, 0.5W:α-Fe_2O_3/MoS_2

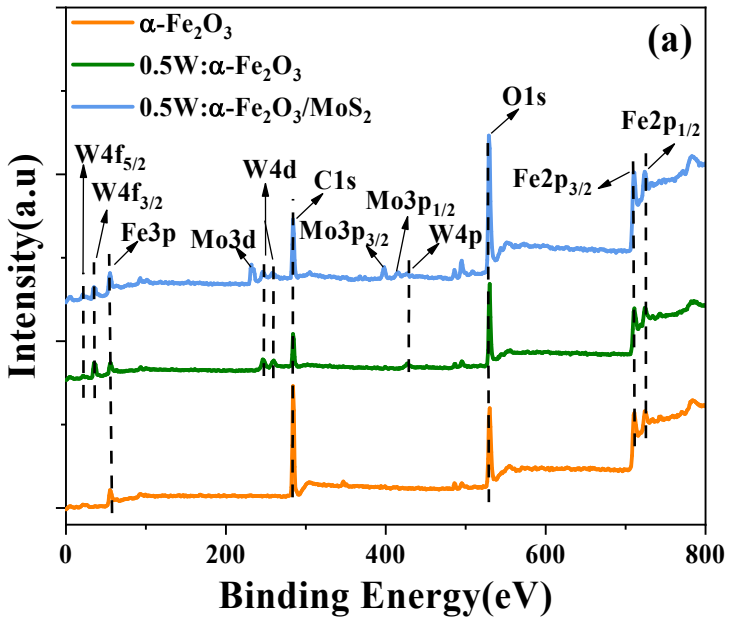

Fig. S3. XPS survey spectra for pure α-Fe_2O_3, 0.5W:α-Fe_2O_3, 0.5W:α-Fe_2O_3/MoS_2.

6. Optical analysis for W doped samples

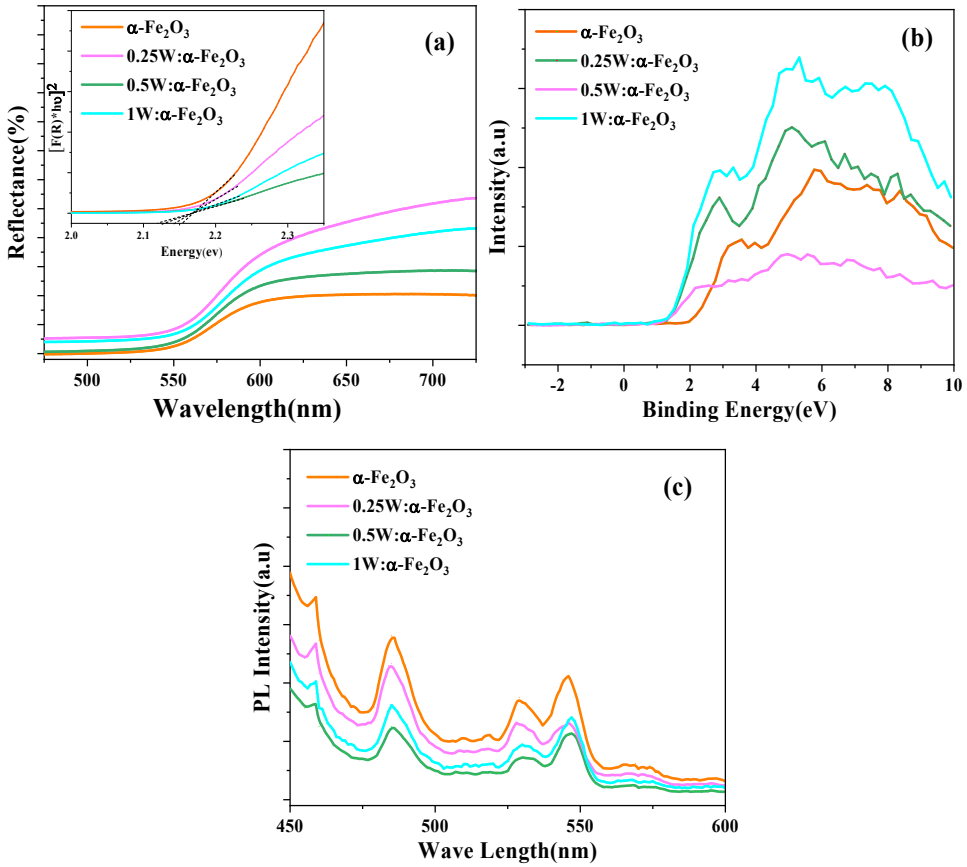

Fig. S4. (a) UV–vis reflectance spectra and band gap energies, (b) XPS for VB, and (c) PL of pure α-Fe_2O_3, 0.25W:α-Fe_2O_3 , 0.5W:α-Fe_2O_3, and 1W:α-Fe_2O_3.

The Tauc equation for direct bandgap thus, can be expressed as in below equation[1],

$(\alpha.h\nu)=A(h\nu-E_g)^{1/2}$

where hν is photon energy, E_g and A is a proportionality constant.

The reflectance is converted into absorption coefficient by using the Kubelka-Munk (K-M) or remission function F(R∞), which gives the final relation equation[1]:

$(F(R).h\nu)=A(h\nu-E_g)^{1/2}$

where hν is photon energy, F(R) is the reflectance of the sample E_g, and A is a proportionality constant.

As shown in Fig. S4a, the band gap for α-Fe_2O_3 decreased after doping W from 2.16 to 2.11 eV. The W:α-Fe_2O_3 samples could absorb more photons than the pristine α-Fe_2O_3 sample could, and

therefore generated more electron-hole pairs. This confirms the improved PEC efficiency under higher wave number (low energy) of visible light irradiation compared with that of pure α-Fe_2O_3.

7. XPS depth profile of the 0.5W: α-Fe_2O_3

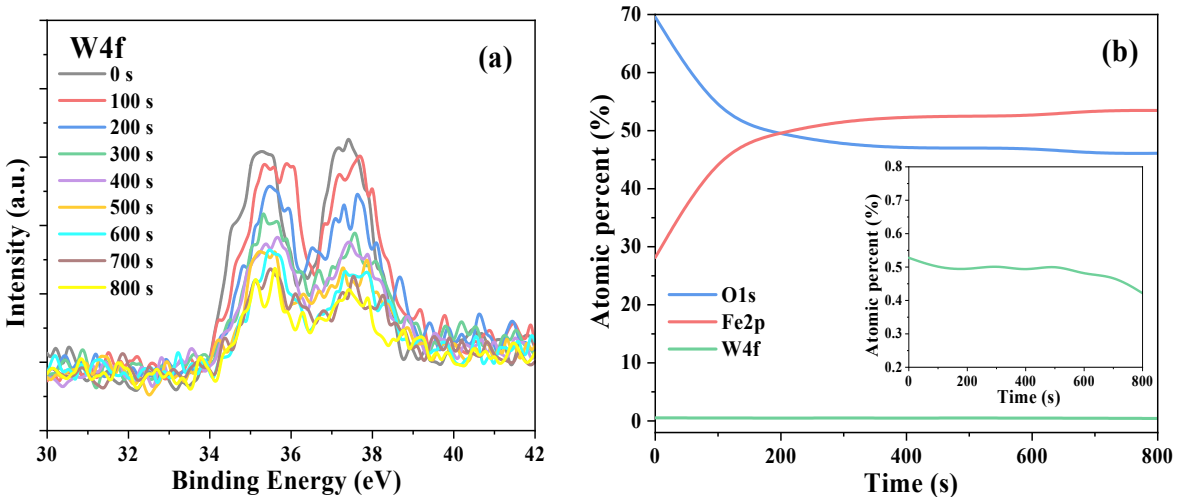

Fig. S5. (a) XPS depth profiles of W4f in different etching times and (b) XPS depth profiles of W4f, Fe2p, and O1s in the 0.5W:α-Fe_2O_3 photoanode.

8. The EPR for detect the defects in the W: α-Fe_2O_3 samples

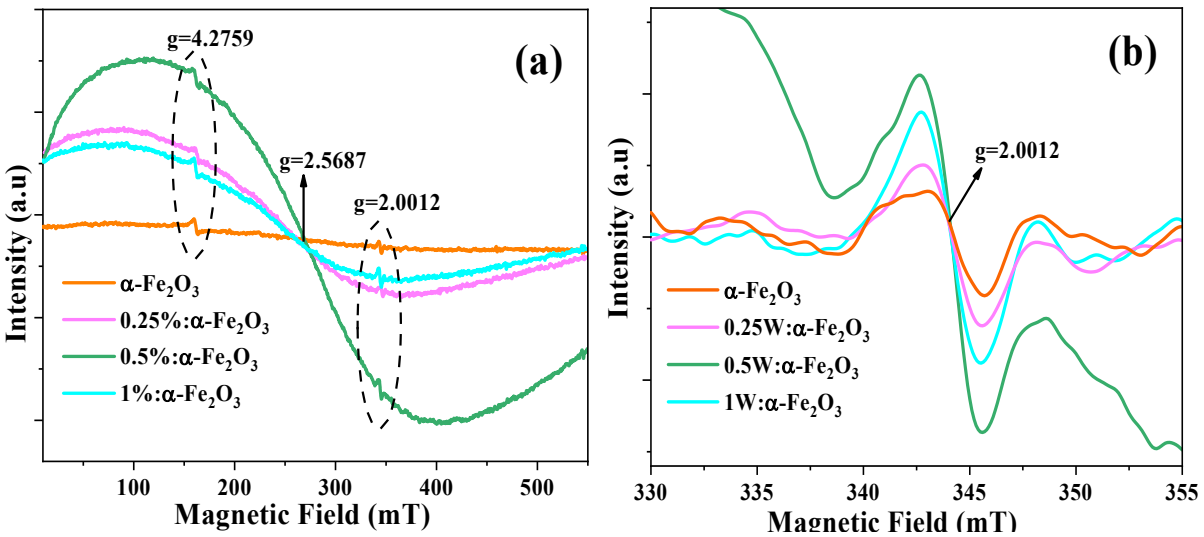

Fig. S6. Electron paramagnetic resonance (EPR) spectra of the pure α-Fe_2O_3, 0.25W:α-Fe_2O_3, 0.5W:α-Fe_2O_3, and 1W:α-Fe_2O_3 photoanodes.

The EPR results of α-Fe_2O_3, 0.25W:α-Fe_2O_3, 0.5W:α-Fe_2O_3, and 1W:α-Fe_2O_3 photoelectrode are shown in Fig. S5. It can be easily seen that the g-values of all sample spectra are the same whereas the peak intensities are enhanced for the W doped α-Fe_2O_3 electrodes. The peak intensity of the EPR spectrum is correlated with the concentration of Fe^{3+} and Fe^{2+} ions, which implies that more oxygen vacancies were produced by the doping process of the tungsten.

9. PEC performance of W doped samples

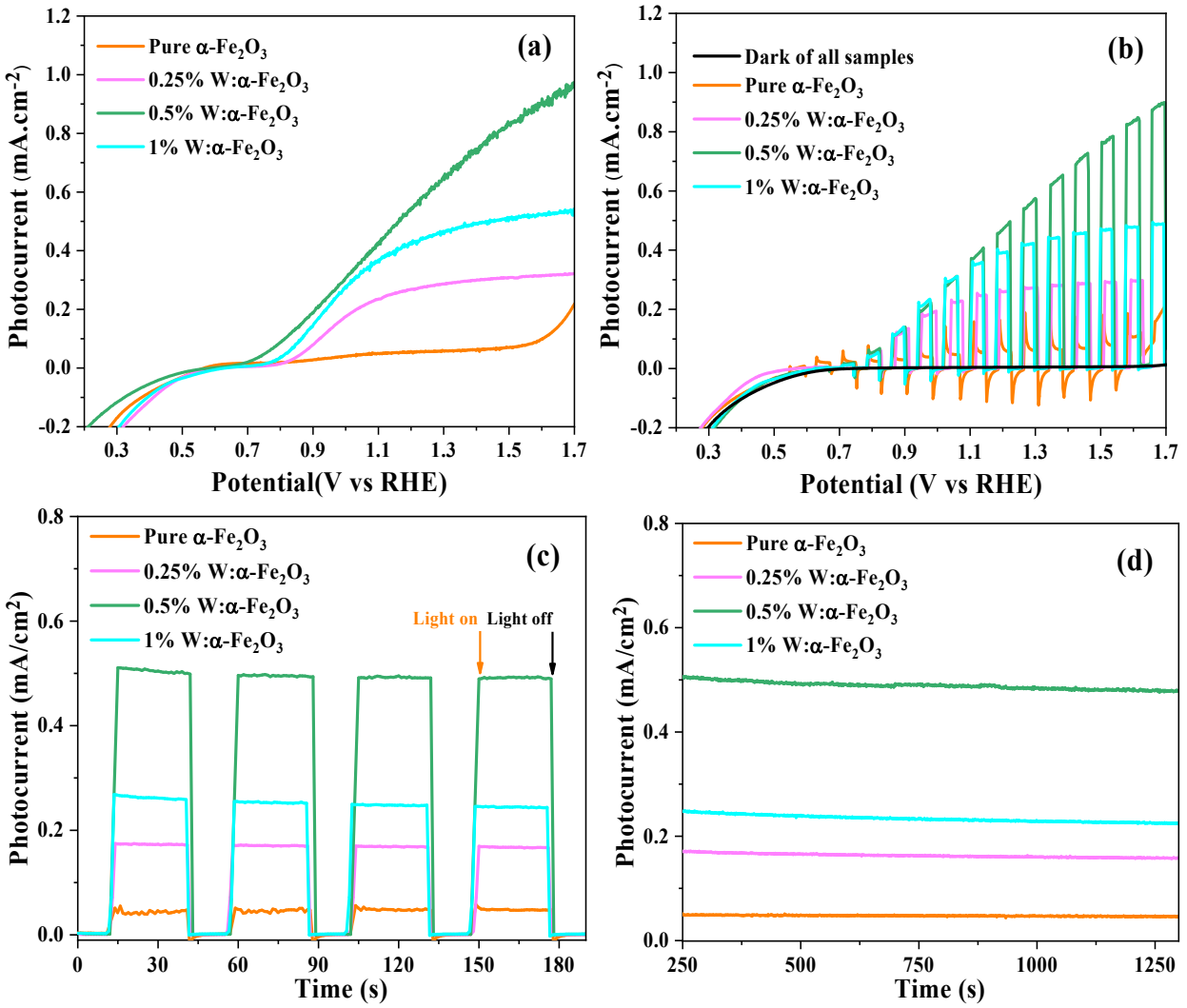

Fig. S7. (a) Linear scan voltammetry and (b) chopped LSV vs. potential linear from 0.3 to 1.5 V vs. RHE, (c) photocurrent response, and (d) photocurrent stability at 1.23 V vs. RHE for pure α-Fe_2O_3, 0.25W:α-Fe_2O_3 , 0.5W:α-Fe_2O_3, and 1W:α-Fe_2O_3 under 100 mWcm^{-2} illumination. The electrolyte was a 1 M NaOH.

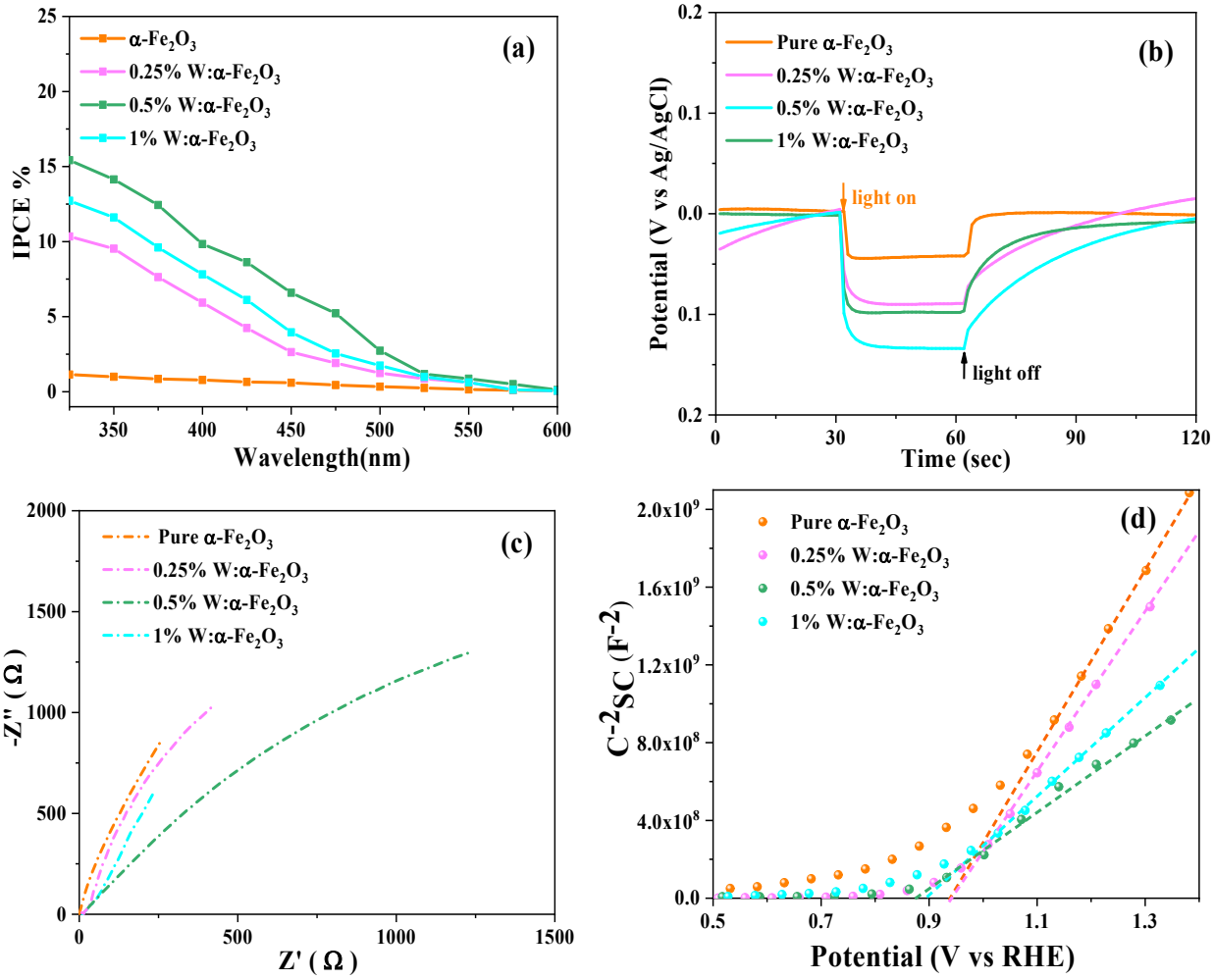

Fig. S8. (a) The incident-photon-to-current-efficiencies (IPCE), (b) change in open circuit potential (ΔOCP) value, (c) Nyquist plot, and . Mott–Schottky analysis for pure α-Fe_2O_3, 0.25W:α-Fe_2O_3 , 0.5W:α-Fe_2O_3, and 1W:α-Fe_2O_3 under 100 $mWcm^{-2}$ illumination. The supporting electrolyte was a 1 M aqueous solution of NaOH.

10. Calculation of V_{fb}, N_D and W_{scl} values

The V_{fb}, N_D and W_{scl} values of photoanodes were calculated with equations (S4):

$$\frac{1}{C^2} = \frac{2}{\varepsilon\varepsilon_0 A^2 e N_D}(\mathrm{V} - V_{fb} - \frac{K_B T}{e})$$

$$Slope = \frac{2}{\varepsilon\varepsilon_0 A^2 e N_D} \rightarrow N_D = \frac{2}{\varepsilon\varepsilon_0 A^2 e(Slope)}$$

$$V_{fb} = \mathrm{int}ercept - \frac{K_B T}{e} \rightarrow \mathrm{int}ercept = V_{fb} + \frac{K_B T}{e}$$

$$\varepsilon = 25 for \alpha - Fe_2O_3 \qquad \varepsilon_0 = 8.854 * 10^{-12} F.m^{-1} \qquad e = 1.6 * 10^{-19} C \qquad K_B = 1.381 * 10^{-23} j.K^{-1} \qquad T = 298K \qquad \text{(S4)}$$

where V is the CB potential (V), V_{fb} the flat band potential (V), k the Boltzmann constant, T the temperature (K), e the charge of an electron (C), ε the relative permittivity, ε_0 the dielectric constant, N_D the donor concentration per unit volume (cm^3), and C_{sc} the surface charge capacitance (F/cm^2). We can obtain qualitative information on donor concentration based on the Mott–Schottky plot in which the positive slopes of the electrodes indicate n-type semiconductors. The width of the space charge layer (W_{SCL}) can be obtained by solving Poisson's equation, using equation (S5).

$$W_{SCL} = \sqrt{\frac{2\varepsilon\varepsilon_0 (V - V_{fb})}{eN_D}} \qquad \text{(S5)}$$

Table S1: V_{fb}, N_D and W_{scl} values of W doped α-Fe_2O_3 with different atomic percentage

Sample	slope	Intercept (X axius)	$N_D(cm^{-3})$	V_{fb}(v)	W_{scl} (nm)
α-Fe_2O_3	5.13E+09	0.94	2.75E+20	0.91	4.64
0.25W:α-Fe_2O_3	4.98E+09	0.94	2.83E+20	0.91	4.57
0.5W:α-Fe_2O_3	2.80E+09	0.87	5.04E+20	0.84	3.37
1W:α-Fe_2O_3	2.86E+09	0.89	4.94E+20	0.86	3.43

Table S2: V_{fb}, N_D and W_{scl} values for α-Fe_2O_3, 0.5W:α-Fe_2O_3 and 0.5W:α-Fe_2O_3/MoS_2

Sample	slope	Intercept (X axius)	N_D (cm^{-3})	V_{fb} (v)	W_{scl} (nm)
α-**Fe_2O_3**	5.13E+09	0.94	2.75E+20	0.91	4.64
0.5W: α-**Fe_2O_3**	2.80E+09	0.87	5.04E+20	0.84	3.37
0.5W: α-**Fe_2O_3/MoS_2**	2.37E+09	0.84	5.97E+20	0.81	3.08

11. The relationship between of V_{fb} and N_D vs. percentage of W doped

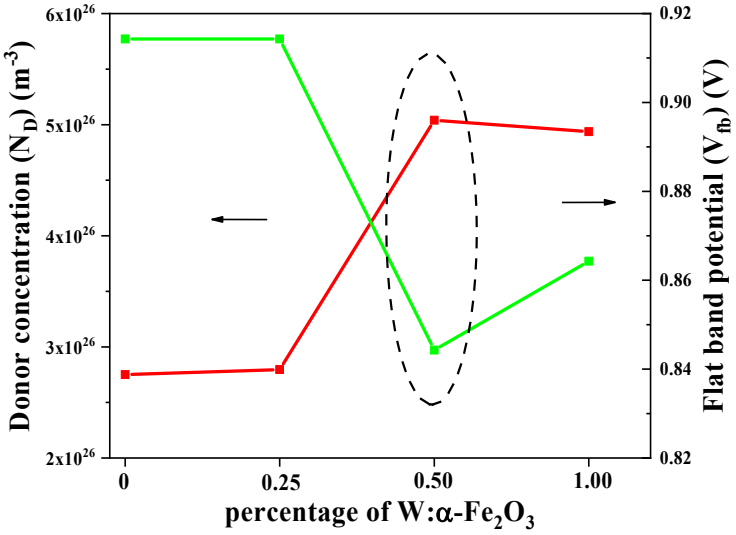

Fig. S9. The relationship between Donor concentration (N_D) and V_{fb}

12. The PEC performance for optimized α-Fe_2O_3/MoS_2

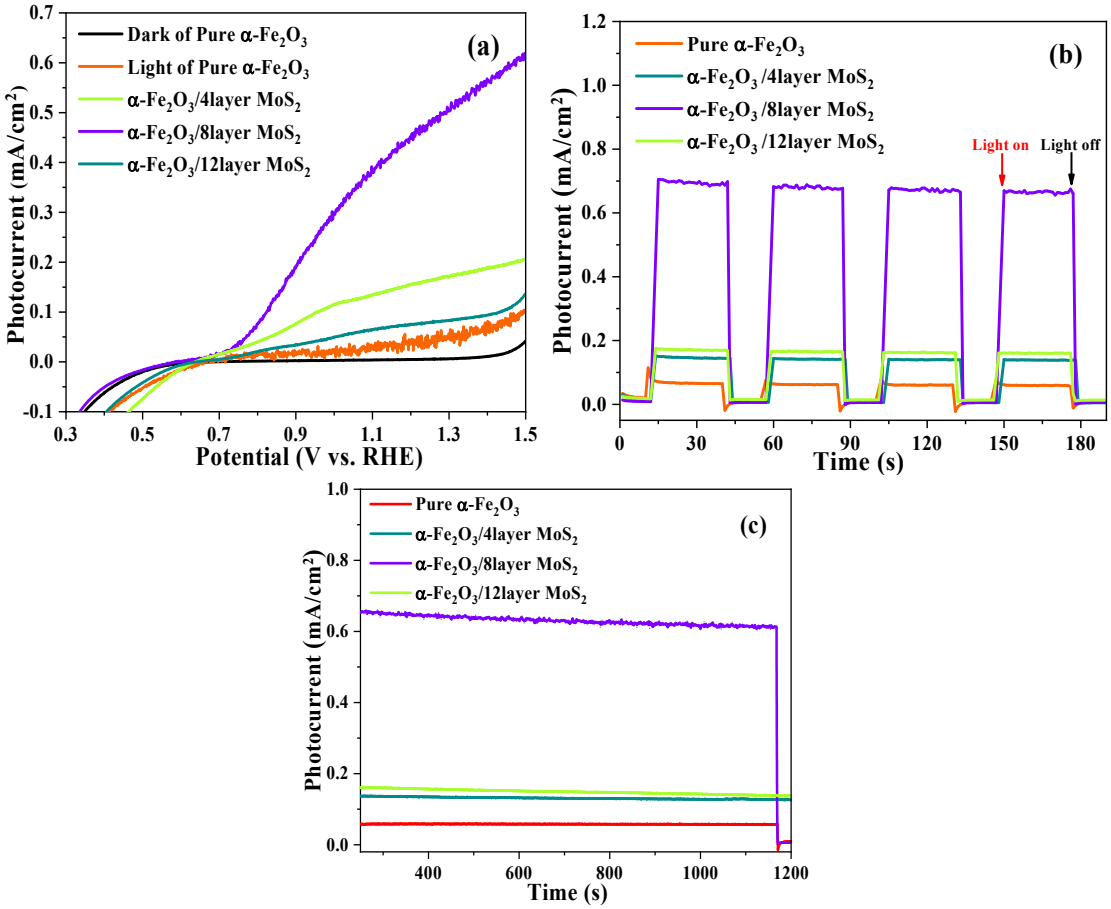

Fig. S10. (a) LSV, (b) photocurrent response, (c) photocurrent stability for pure α-Fe_2O_3, α-Fe_2O_3/4layerMoS_2, α-Fe_2O_3/8layerMoS_2, and α-Fe_2O_3/12layerMoS_2 under 100 $mWcm^{-2}$ illumination in 1 M NaOH.

The LSV of the α-Fe_2O_3 α-Fe_2O_3/4layer MoS_2, α-Fe_2O_3/8layer MoS_2, and α-Fe_2O_3/12layer MoS_2 electrodes were measured between 0.3 and 1.5 V vs. RHE, as shown in Fig. S11a. The photocurrent density significantly increased after the deposition of MoS_2 nanosheets with the highest value of 0.7 $mA.cm^{-2}$ at 1.5 V vs. RHE for α-Fe_2O_3/8layer MoS_2. Chronoamperometry scans for 4 cycles (Fig. S11b), measured under intermittent irradiation (30 min light on and 15 min light off) confirm the photocurrent responses. The fast and uniform reactions to each light on/off interval of the electrodes reflect the good producibility of the samples. As shown in Fig. S11c, the photocurrent stabilities of different α-Fe_2O_3/MoS_2 films were obtained by continuous illumination after 10 on-off cycles. The photoelectrodes showed stable photocurrent, even in 15-min light illumination, without a significant downturn. These behaviors may possibly be attributable to the heterojunction between MoS_2 and α-Fe_2O_3, which improved the charge separation and reduced the recombination of photogenerated electrons and holes [2]. Therefore, the optimum concentration of MoS_2 on the surface of each electrode is 800 mL (8times×each time amount (100ml)) which loaded on the optimum W doped α-Fe_2O_3 electrodes.

13. The LSV and chopped LSV for optimized all of W:α-Fe_2O_3/MoS_2

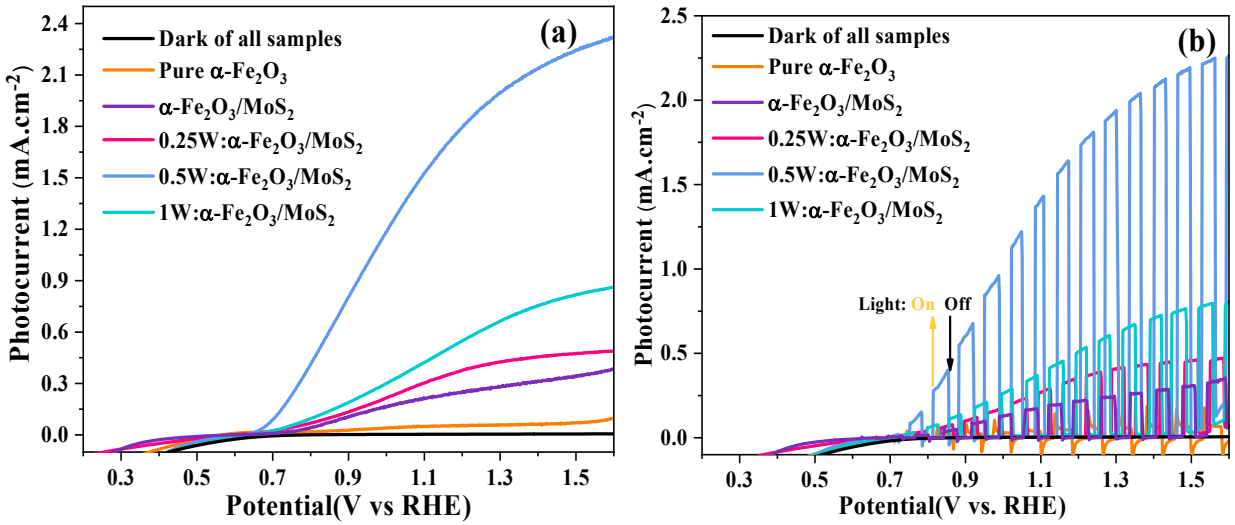

Fig. S11. (a)Linear scan voltammetry and (b)chopped LSV vs. potential from 0.3 to 1.5 V (vs. RHE) for pure α-Fe_2O_3, α-Fe_2O_3/MoS_2, 0.25W:α-Fe_2O_3/MoS_2 , 0.5W:α-Fe_2O_3/MoS_2, and 1W:α-Fe_2O_3/MoS_2 under 100 $mWcm^{-2}$ illumination. The electrolyte was a 1 M NaOH.

14. LSV for comparison the photocurrent density vs. potential

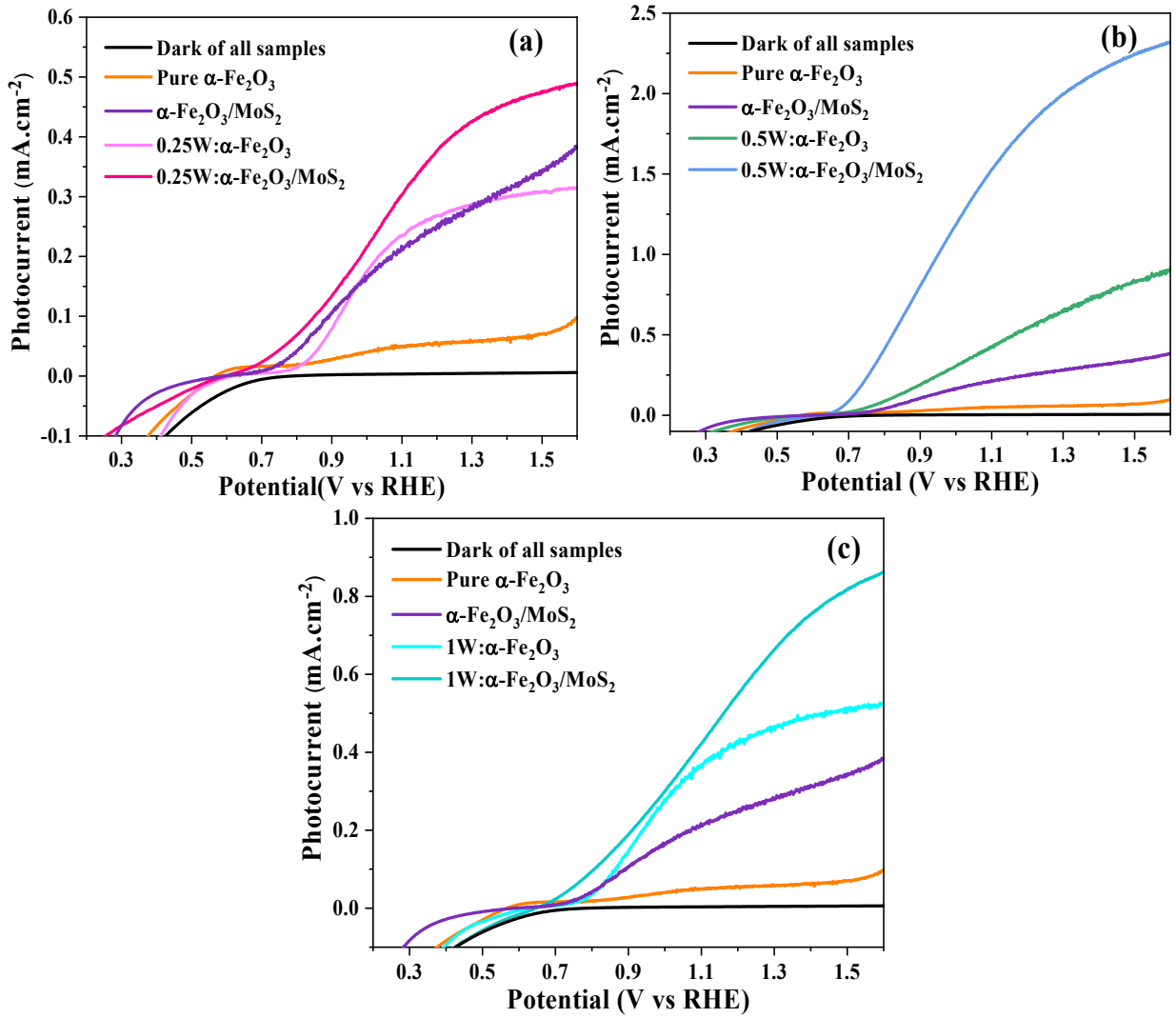

Fig. S12. Linear scan voltammetry (LSV) for comparison the photocurrent density vs. potential from 0.3 to 1.5 V (vs. RHE) of (a) pure α-Fe_2O_3, α-Fe_2O_3/MoS_2, 0.25W:α-Fe_2O_3, and 0.25W:α-Fe_2O_3/MoS_2 , (b) pure α-Fe_2O_3, α-Fe_2O_3/MoS_2, 0.5W:α-Fe_2O_3, and 0.5W:α-Fe_2O_3/MoS_2, and (c) pure α-Fe_2O_3, α-Fe_2O_3/MoS_2, 1W:α-Fe_2O_3, and 1W:α-Fe_2O_3/MoS_2 under 100 $mWcm^{-2}$ illumination. The electrolyte was a 1 M NaOH.

15. Calculation of τ value in TRPL

The time-resolved photoluminescence (TRPL) curves shown in Fig.6d in the manuscript, assess recombination kinetics of photoinduced electron-hole pairs. TRPL decay spectrum was fitted with a biexponential decay function displayed as Eq. (S6)[3]:

$$\text{PL (t)} = A_1 e^{-\frac{t}{\tau_1}} + A_2 e^{-\frac{t}{\tau_2}} + \text{y0} \quad \text{(S6)}$$

Where τ_i is the decay time, K is a constant for the baseline offset, and A_i is the decay amplitude. The fitting parameters are summarized in Table S3. The average emission time also was calculated based on Eq. (S7)[3]:

$$\tau = \frac{A_1\tau_1^2 + A_2\tau_2^2}{A_1\tau_1 + A_2\tau_2} \quad \text{(S7)}$$

Table S3. Biexponential of the PL decay of pure α-Fe_2O_3, 0.5W:α-Fe_2O_3, and 0.5W:α-Fe_2O_3/MoS_2

Parameters / **Samples**	**α-Fe_2O_3**	**0.5W:α-Fe_2O_3**	**0.5W:α-Fe_2O_3/MoS_2**
y0	0.00	0.01	0.01
A_1	0.07	0.34	0.23
τ_1	0.41	1.83	3.28
A_2	0.19	0.18	1.05
τ_2	0.28	1.75	1.98
Avg lifetime (ns)	0.32	1.80	2.33

16. Calculation of η_{inj} and η_{sep} values

The J_{abs} (the photocurrent density achievable assuming 100% absorbed photon-to-current conversion efficiency for photons) was calculated by the solar spectral irradiance at AM 1.5G ($W \cdot m^{-2} \cdot nm^{-1}$, ASTM G173−03) which is first converted to solar photocurrents vs. wavelength ($A \cdot m^{-2} \cdot nm^{-1}$) assuming 100% IPCE for photons. Further, the solar photocurrents are multiplied by the light-harvesting efficiency (LHE) at each wavelength. By adding these products up, J_{abs} for pure α-Fe_2O_3, 0.5%W:α-Fe_2O_3 and 0.5%W:α-Fe_2O_3/MoS_2 is calculated to be 9.1, 7.87 and 7.56 mA/cm^2. Further, charge separation and injection efficiencies were measured using a 0.5 M H_2O_2 hole scavenger added to 1 M NaOH electrolyte solution [4, 5].

The water-splitting photocurrent (J_{H2O}) is a product of the rate of photon absorption expressed as a current density (J_{abs}) and the highest J_{abs}, can be calculated by the following equations S8 and S9 [6]:

$$J_{abs}=\int_{200nm}^{800nm} \frac{\lambda}{1240} \times \eta_{LHE}(\lambda) \times AM1.5\psi(\lambda) d\lambda \quad \text{(S8)}$$

$$\eta_{LHE}(\lambda) = 1 - 10^{-A(\lambda)} \quad \text{(S9)}$$

Where $\eta_{LEH}(\lambda)$, AM 1.5ψ(λ), and A(λ) refer to the light-harvesting efficiency, AM 1.5 simulated solar spectral irradiance, and absorbance at a specific wavelength, respectively. Furthermore, the charge separation efficiency of the photogenerated carriers (η_{sep}), and the charge injection efficiency to the electrolyte (η_{inj}) are calculated by equations S10, S11, and S12 under different applied biases using a widely accepted hole scavenger approach[7].

$$\eta_{inj} = J_{H2O} / J_{H2O2} \quad \text{(S10)}$$

$$\eta_{sep} = J_{H2O2} / J_{abs} \quad \text{(S11)}$$

$$J_{H2O} = J_{abs} \times \eta_{sep} \times \eta_{inj} \quad \text{(S12)}$$

Where J_{H2O} and J_{H2O2} refer to the photocurrent density measured in the electrolytes of 1 M NaOH and 1 M NaOH + 0.5 M H_2O_2, respectively.

17. Energy band diagram from UPS

Energies of the Fermi levels (E_F) and the valence band maxima (E_{VBM}) retrieved from ultraviolet photoelectron spectroscopy (UPS) spectra show in Fig. S13. The work function (Φ) gives the energy of the Fermi level with respect to the vacuum level and is calculated with Eq. (S13):

$$\Phi = h\nu - E_{highcutoff} \quad ,(h\nu \approx 21.22 \text{ ev}) \tag{S13}$$

$|E_{VBM}|$ is calculated with Eq. (S14):

$$|E_{VBM}| = h\nu - (E_{highcutoff} - E_{lowcutoff}) \tag{S14}$$

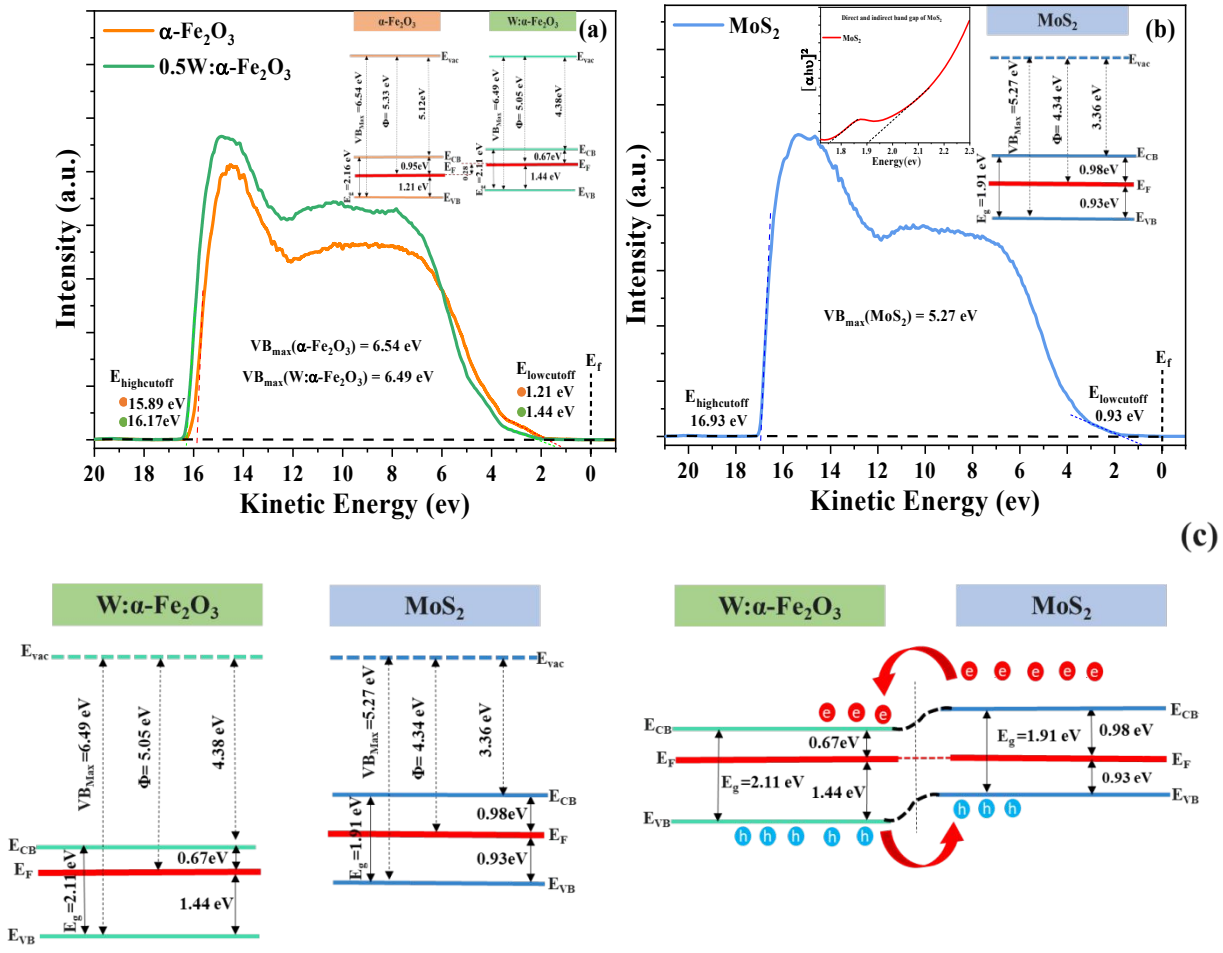

Fig. S13. UPS and work function of (a) pure hematite and 0.5W doped , (b) MoS_2, and (c) energy band diagram of the heterojunction.

18. Calculation of the geometry for nanorods

In the based α-Fe_2O_3 nanorods structures, a circular depletion layer will grow from the surface towards the center of the rod at changing bias potential, and the geometry may represent significant changes with respect to Eq.(S4) that we considered in the section 10. Each nanorod is described as a cylinder of radius R with axial symmetry and donor density N_D. The Poisson equation is solved in the depletion approximation for the voltage V. In Eq. (S15) [8],

$$\frac{1}{r}\frac{\partial}{\partial r}\left(r\frac{\partial V}{\partial r}\right) = -\frac{q}{\varepsilon_0\varepsilon_r}N_D \quad \text{(S15)}$$

ε_r is the dielectric constant of the α-Fe_2O_3 nanorods, ε_0 is the dielectric constant, N_D is the donor concentration per unit volume (cm^3), and q is the positive elementary charge. The central zone of the cylinder is a neutral region of electron density with radius x, and the surface $x \leqslant r \leqslant R$ is a region of positive space charge qN_D. The voltage in the quasineutral region V_{sc}, that coincides with the total voltage drop across the barrier, is estimated by Eq. (S16)[8]:

$$V_{sc} = -\frac{N_D}{2\varepsilon_0\varepsilon_r}q\left(\frac{1}{2}(R^2 - x^2) + R^2\, ln(\frac{x}{R})\right) \quad \text{(S16)}$$

Estimated of different quantities for nanorods of radius R and length around 42 and 120 (for 0.5%W:α-Fe_2O_3/MoS_2 150 nm) from the SEM images, respectively. Radius of the neutral region vs. the potential drop across the depletion layer was calculated for pure α-Fe_2O_3, 0.5%W:α-Fe_2O_3 and 0.5%W:α-Fe_2O_3/MoS_2 samples by using the Mott-Schottky data and above equations that shows in Fig. S14.

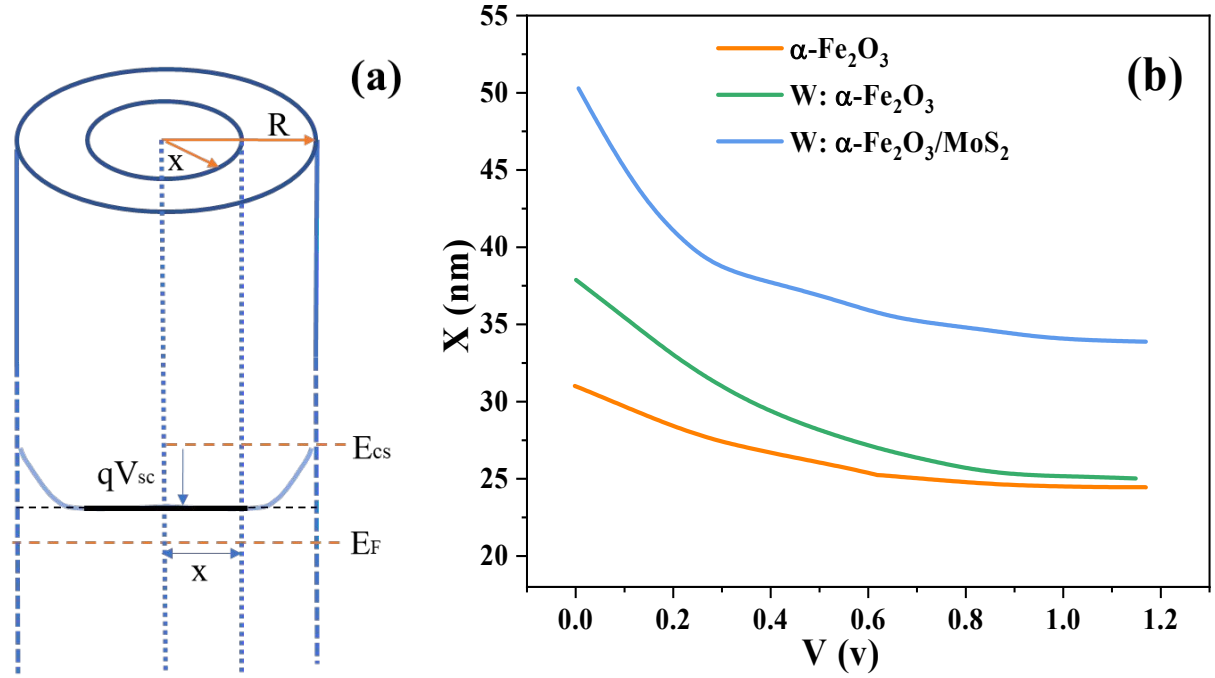

Fig. S14. (a) Schematic of the radial direction of a nanorod indicating the depletion layer at the surface and the quasineutral region of radius x in the center. (b) Radius of the neutral region vs barrier voltage for pure α-Fe_2O_3, 0.5%W:α-Fe_2O_3 and 0.5%W:α-Fe_2O_3/MoS_2 electrodes.

19. Hydrogen and Oxygen Evolution Measurement:

For overall water splitting of α-Fe_2O_3, 0.5W:α-Fe_2O_3 and 0.5Wα-Fe_2O_3 /MoS_2 photoanodes was evaluated by measuring the H_2 and O_2 evolution at 1.23 V versus RHE under 100 mW.cm^{-2} irradiations in 1M of NaOH electrolyte. The produced hydrogen and oxygen gas amounts were measured using the gas chromatography (GC). Before starting the water splitting reaction nitrogen gas was purged into cell for 2 h to remove the air remaining in the reaction vessel. The light source was turned on and the amounts of evolved oxygen and hydrogen were measured by a tight syringe every 20 min using a gas chromatograph for 2h. The gas samples were injected in the GC, and the resulting peak areas (AreaH_2, AreaO_2) were recorded. The evolved hydrogen-oxygen gases were calculated according to the following formula[9, 10]:

$$H_2(or\ O_2)\mu mol.cm^{-2} = \left(\frac{Area\ of\ H_2(or\ O_2)peak}{Slope\ of\ calibration\ curve}\right) \times (Head\ space\ volume) \times \left(\frac{1mol}{24.2\ L}\right) \quad \text{(S17)}$$

The detailed calculation process for the Faradaic efficiency was shown as following:

Faradic efficiency = Actual photocurrent density/ Theoretical photocurrent density (S18)

Actual photocurrent density = N× nH_2/O_2 × F (S19)

F is the Faraday constant which is 0.096487 C/μmol). nH_2/O_2 (μmol) is amount of H_2 or O_2 evolution determined by gas chromatography. N is number of electrons needed to evolve one molecule of H_2 or O_2. It is assumed that 2 electrons are needed to produce one molecule of H_2, and 4 electrons are needed for one molecule of O_2.

Theoretical photocurrent density= Q = I × t (S20)

Q is quantity of charge (electricity) in coulombs (C). I is current in amperes (amps, A) and t is time (seconds).

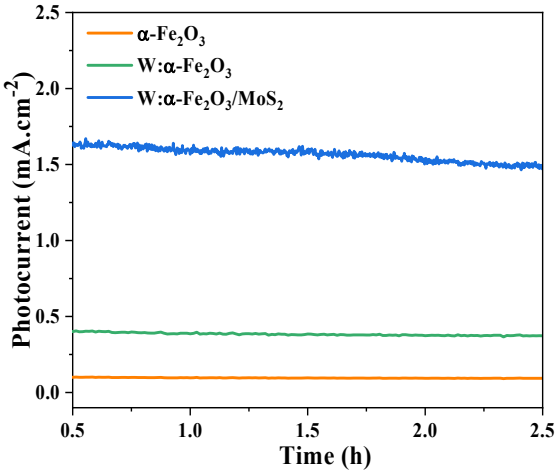

Fig.S15. photocurrent stability at 1.23 V (vs. RHE) for pure α-Fe_2O_3, 0.5W:α-Fe_2O_3, and 0.5W:α-Fe_2O_3/MoS_2 under 100 $mWcm^{-2}$ illumination. The electrolyte was a 1 M NaOH.

20. Some of the recent reported doped hematite photoanodes with/without heterojunction

Table S4. Recently reported doped hematite photoanodes with/without heterojunction or cocatalysts

Photoanode	**Conditions**	**Photocurrent density (1.23 V vs RHE)**	**Reference**
Ti-Fe_2O_3/10-MoSx	1 M NaOH AM 1.5G (100 mW.cm^{-2})	~1.7 mA.cm^{-2}	(2015)[11]
Dual-regrowth Fe_2O_3/with NiFeOx	0.5 M Phosphate solution AM 1.5G (100 mW.cm^{-2})	~1.3 mA.cm^{-2}	(2015)[12]
SnO_2-SiO*x*/Ti:Fe_2O_3/with FeOOH	1 M NaOH AM 1.5G (100 mW.cm^{-2})	~1.54 mA.cm^{-2}	(2016)[13]
W-Fe_2O_3	1 M NaOH AM 1.5G (100 mW.cm^{-2})	~0.27 mA.cm^{-2}	(2016)[14]
Ti:Fe_2O_3/NiPi	0.25 M Na_3PO_4 AM 1.5G (100 mW.cm^{-2})	~1.3 mA.cm^{-2}	(2017)[15]
Fe_2O_3/with F:FeOOH/FeNiOOH	1 M NaOH AM 1.5G (100 mW.cm^{-2})	~1.05 mA.cm^{-2}	(2018)[16]
α-Fe_2O_3/RGO/Ag	1 M KOH AM 1.5G (100 mW.cm^{-2})	~0.72 mA.cm^{-2}	(2018)[17]
P:Fe_2O_3/MnO_2	1 M KOH AM 1.5G (100 mW.cm^{-2})	~1.65 mA.cm^{-2}	(2018)[18]
P-Fe_2O_3/Ce-Pi	1 M NaOH AM 1.5G (100 mW.cm^{-2})	~1.24 mA.cm^{-2}	(2019)[19]
Mn:Fe_2O_3/Ti:Fe_2O_3	1 M NaOH AM 1.5G (100 mW.cm^{-2})	~1.2 mA.cm^{-2}	(2020)[20]
Ti-Co-MOF (ZIF-67) on Fe_2O_3	1 M KOH AM 1.5G (100 mW.cm^{-2})	~1 mA.cm^{-2}	(2020)[21]
α-Fe_2O_3/MoS_2	1 M KOH AM 1.5G (100 mW.cm^{-2})	~0.8 mA.cm^{-2}	(2021)[22]
0.5%W:α-Fe_2O_3/MoS_2	1 M NaOH AM 1.5G (100 mW.cm^{-2})	**~1.83 mA.cm^{-2}**	**This Work**

Reference:

1. Jubu, P. R.; Yam, F. K.; Igba, V. M.; Beh, K. P., Tauc-plot scale and extrapolation effect on bandgap estimation from UV–vis–NIR data – A case study of β-Ga2O3. *J. Solid State Chem.* **2020,** *290*, 121576.
2. Bhat, S. S.; Pawar, S. A.; Potphode, D.; Moon, C.-K.; Suh, J. M.; Kim, C.; Choi, S.; Patil, D. S.; Kim, J.-J.; Shin, J. C. J. A. C. B. E., Substantially enhanced photoelectrochemical performance of TiO2 nanorods/CdS nanocrystals heterojunction photoanode decorated with MoS2 nanosheets. **2019,** *259*, 118102.
3. Guo, Y.; Liu, T.; Wang, N.; Luo, Q.; Lin, H.; Li, J.; Jiang, Q.; Wu, L.; Guo, Z., Ni-doped α-Fe2O3 as electron transporting material for planar heterojunction perovskite solar cells with improved efficiency, reduced hysteresis and ultraviolet stability. *Nano Energy* **2017,** *38*, 193-200.
4. Dotan, H.; Sivula, K.; Grätzel, M.; Rothschild, A.; Warren, S. C., Probing the photoelectrochemical properties of hematite (α-Fe2O3) electrodes using hydrogen peroxide as a hole scavenger. *Energy & Environmental Science* **2011,** *4* (3), 958-964.
5. Zhang, K.; Ma, M.; Li, P.; Wang, D. H.; Park, J. H., Water Splitting Progress in Tandem Devices: Moving Photolysis beyond Electrolysis. *Advanced Energy Materials* **2016,** *6* (15), 1600602.
6. Bassi, P. S.; Antony, R. P.; Boix, P. P.; Fang, Y.; Barber, J.; Wong, L. H., Crystalline Fe2O3/Fe2TiO5 heterojunction nanorods with efficient charge separation and hole injection as photoanode for solar water oxidation. *Nano Energy* **2016,** *22*, 310-318.
7. Lei, B.; Xu, D.; Wei, B.; Xie, T.; Xiao, C.; Jin, W.; Xu, L., In Situ Synthesis of α-Fe2O3/Fe3O4 Heterojunction Photoanode via Fast Flame Annealing for Enhanced Charge Separation and Water Oxidation. *ACS Applied Materials & Interfaces* **2021,** *13* (3), 4785-4795.
8. Mora-Seró, I.; Fabregat-Santiago, F.; Denier, B.; Bisquert, J.; Tena-Zaera, R.; Elias, J.; Lévy-Clément, C., Determination of carrier density of ZnO nanowires by electrochemical techniques. *Applied Physics Letters* **2006,** *89* (20), 203117.
9. Tayebi, M.; Tayyebi, A.; Lee, B.-K.; Lee, C.-H.; Lim, D.-H., The effect of silver doping on photoelectrochemical (PEC) properties of bismuth vanadate for hydrogen production. *Sol. Energy Mater. Sol. Cells* **2019,** *200*, 109943.
10. Tayebi, M.; Lee, B.-K., The effects of W/Mo-co-doped BiVO4 photoanodes for improving photoelectrochemical water splitting performance. *Catalysis Today* **2021,** *361*, 183-190.
11. Ahn, H.-J.; Yoon, K.-Y.; Kwak, M.-J.; Lee, J.-S.; Thiyagarajan, P.; Jang, J.-H., MoSx supported hematite with enhanced photoelectrochemical performance. *Journal of Materials Chemistry A* **2015,** *3* (43), 21444-21450.
12. Jang, J.-W.; Du, C.; Ye, Y.; Lin, Y.; Yao, X.; Thorne, J.; Liu, E.; McMahon, G.; Zhu, J.; Javey, A.; Guo, J.; Wang, D., Enabling unassisted solar water splitting by iron oxide and silicon. *Nature Communications* **2015,** *6* (1), 7447.
13. Cho, I. S.; Han, H. S.; Logar, M.; Park, J.; Zheng, X., Enhancing Low-Bias Performance of Hematite Photoanodes for Solar Water Splitting by Simultaneous Reduction of Bulk, Interface, and Surface Recombination Pathways. *Advanced Energy Materials* **2016,** *6* (4), 1501840.
14. Su, J.; Wang, J.; Liu, C.; Feng, B.; Chen, Y.; Guo, L., On the role of metal atom doping in hematite for improved photoelectrochemical properties: a comparison study. *RSC Advances* **2016,** *6* (104), 101745-101751.
15. Wang, J.; Yang, J.; Zheng, Z.; Lu, T.; Gao, W., The role of thin NiPi film for enhancing solar water splitting performance of Ti doped hematite. *Applied Catalysis B: Environmental* **2017,** *218*, 277-286.

16. Deng, J.; Zhang, Q.; Feng, K.; Lan, H.; Zhong, J.; Chaker, M.; Ma, D., Efficient Photoelectrochemical Water Oxidation on Hematite with Fluorine-Doped FeOOH and FeNiOOH as Dual Cocatalysts. *ChemSusChem* **2018,** *11* (21), 3783-3789.
17. Yu, L.; Zhang, Y.; He, J.; Zhu, H.; Zhou, X.; Li, M.; Yang, Q.; Xu, F., Enhanced photoelectrochemical properties of α-Fe2O3 nanoarrays for water splitting. *Journal of Alloys and Compounds* **2018,** *753*, 601-606.
18. Rui, Q.; Wang, L.; Zhang, Y.; Feng, C.; Zhang, B.; Fu, S.; Guo, H.; Hu, H.; Bi, Y., Synergistic effects of P-doping and a MnO2 cocatalyst on Fe2O3 nanorod photoanodes for efficient solar water splitting. *Journal of Materials Chemistry A* **2018,** *6* (16), 7021-7026.
19. Bu, X.; Gao, Y.; Zhang, S.; Tian, Y., Amorphous cerium phosphate on P-doped Fe2O3 nanosheets for efficient photoelectrochemical water oxidation. *Chemical Engineering Journal* **2019,** *355*, 910-919.
20. Tao, S.-M.; Lin, L.-Y., Design of efficient Mn-doped α-Fe2O3/Ti-doped α-Fe2O3 homojunction for catalyzing photoelectrochemical water splitting. *International Journal of Hydrogen Energy* **2020,** *45* (11), 6487-6499.
21. Li, W.; Wang, K.; Yang, X.; Zhan, F.; Wang, Y.; Liu, M.; Qiu, X.; Li, J.; Zhan, J.; Li, Q.; Liu, Y., Surfactant-assisted controlled synthesis of a metal-organic framework on Fe2O3 nanorod for boosted photoelectrochemical water oxidation. *Chemical Engineering Journal* **2020,** *379*, 122256.
22. Masoumi, Z.; Tayebi, M.; Lee, B.-K., Ultrasonication-assisted liquid-phase exfoliation enhances photoelectrochemical performance in α-Fe2O3/MoS2 photoanode. *Ultrasonics Sonochemistry* **2021,** *72*, 105403.